Biomaterials 305 (2024) 122465

Contents lists available at ScienceDirect

Biomaterials

journal homepage: www.elsevier.com/locate/biomaterials

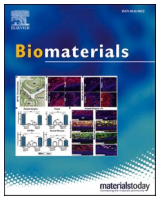

Bioactive mesoporous silica nanoparticle-functionalized titanium implants with controllable antimicrobial peptide release potentiate the regulation of inflammation and osseointegration

Jiyu Dong [a,1], Fangman Chen [a,d,1], Yuying Yao [b,c,1], Congcong Wu [e], Silin Ye [b,c], Zunwei Ma [a], Haipeng Yuan [b,c], Dan Shao [a,c,d,**], Lin Wang [a,b,c,*], Yingjun Wang [a,c,***]

[a] National Engineering Research Center for Tissue Restoration and Reconstruction, South China University of Technology, Guangzhou 510006, China
[b] School of Material Science and Engineering, South China University of Technology, Guangzhou 510006, China
[c] Key Laboratory of Biomedical Engineering of Guangdong Province, South China University of Technology, Guangzhou 510006, China
[d] School of Medicine, South China University of Technology, Guangzhou 510006, China
[e] Jinan Center for Disease Control and Prevention, Jinan 250001, China

ARTICLE INFO

Keywords:
Mesoporous silica nanoparticle
Antimicrobial peptide
Titanium
Macrophages
Osseointegration

ABSTRACT

Bacterial infection and delayed osseointegration are two major challenges for titanium-based orthopedic implants. In the present study, we developed a functionalized titanium implant Ti-M@A by immobilizing antimicrobial peptide (AMP) HHC36-loaded diselenide-bridged mesoporous silica nanoparticles (MSNs) on the surface, which showed good long-term and mechanical stability. The functionalized implants can realize the sustained release of AMP over 30 days and exhibit over 95.71 % antimicrobial activity against four types of clinical bacteria (*S. aureus*, *E. coli*, *P. aeruginosa* and *MRSA*), which arose from the capability to destroy the bacterial membranes. Moreover, Ti-M@A can efficiently inhibit the biofilm formation of the bacteria. The functionalized implants can also significantly promote the osteogenic differentiation of *mouse bone marrow-derived mesenchymal stem cells* (*mBMSCs*) because of the Se in MSNs. Notably, it can trigger macrophages toward M2 polarization *in vitro* by scavenging ROS in LPS-activated macrophages. Consequently, *in vivo* assays with infection and non-infection bone defect models demonstrated that such bioactive implants can not only kill over 98.82 % of *S. aureus*, but also promote osseointegration. Hence, this study provides a combined strategy to resolve bacterial infection and delayed osseointegration for titanium implants.

1. Introduction

Titanium-based materials have been widely used as orthopedic implants in the clinic [1] due to their excellent mechanical properties [2], biocompatibility [3] and corrosion resistance [4]. However, bacterial infection and delayed osseointegration are still two major problems that remain with the use of titanium implants due to their bioinert surface [5]. Biomaterial-associated infection (BAI) is a serious global problem [6,7], accounting for 4 %–15 % of nosocomial infections worldwide [8,9]. BAIs have serious consequences, including surgical failure, disability, sepsis and even patient death [10–12]. Once infection occurs, pathogens tend to accumulate on the implant surface and form biofilms to protect themselves from immune defenses and environmental pressure [13]. Therefore, it is extremely difficult to treat bacterial infections of implants. On the other hand, delayed osseointegration can lead to loosening, accompanied by the production of wear particles to trigger inflammatory reactions and bacterial infection [14]. It has been reported that approximately 18 % of clinical implant failures are caused by aseptic loosening [15]. Notably, these two problems, i.e., bacterial infection and delayed osseointegration, reinforce each other and

* Corresponding author. National Engineering Research Center for Tissue Restoration and Reconstruction, South China University of Technology, Guangzhou 510006, China.
** Corresponding author. School of Medicine, South China University of Technology, Guangzhou 510006, China.
*** Corresponding author. Key Laboratory of Biomedical Engineering of Guangdong Province, South China University of Technology, Guangzhou 510006, China.
E-mail addresses: shaodan@scut.edu.cn (D. Shao), wanglin3@scut.edu.cn (L. Wang), imwangyj@scut.edu.cn (Y. Wang).
[1] These authors contributed equally to this work.

https://doi.org/10.1016/j.biomaterials.2023.122465
Received 8 September 2023; Received in revised form 23 December 2023; Accepted 31 December 2023
Available online 2 January 2024

together lead to a high rate of implant failure.

Functionalizing the implant surface is an efficient strategy to overcome these problems. To prevent bacterial infection, various antibacterial agents can be immobilized on the implant surface. Common incorporated agents include metal ions/nanoparticles (*e.g.*, silver, copper, zinc or gold) [16–19] and antibiotics (*e.g.*, cephalothin, carbenicillin, amoxicillin or vancomycin) [20–23]. However, the potential toxicity of metals and drug resistance of antibiotics limit their application. Recently, antimicrobial peptides (AMPs) have become promising candidates because of their broad-spectrum antibacterial properties and low drug resistance [24–26]. In particular, some short AMPs, *e.g.*, the rationally designed peptide HHC36 (sequence: Lys-Arg-Trp-Trp-Lys-Trp-Trp-Arg-Arg), exhibited excellent antibacterial activity against common clinical bacteria [27,28]. Increasing physical and chemical methods have been developed to anchor AMPs onto titanium implant surfaces [27,29], such as physical adsorption [30] and covalent binding [31–33]. On the one hand, the physical adsorption method may not be effective for an extended period of time due to the

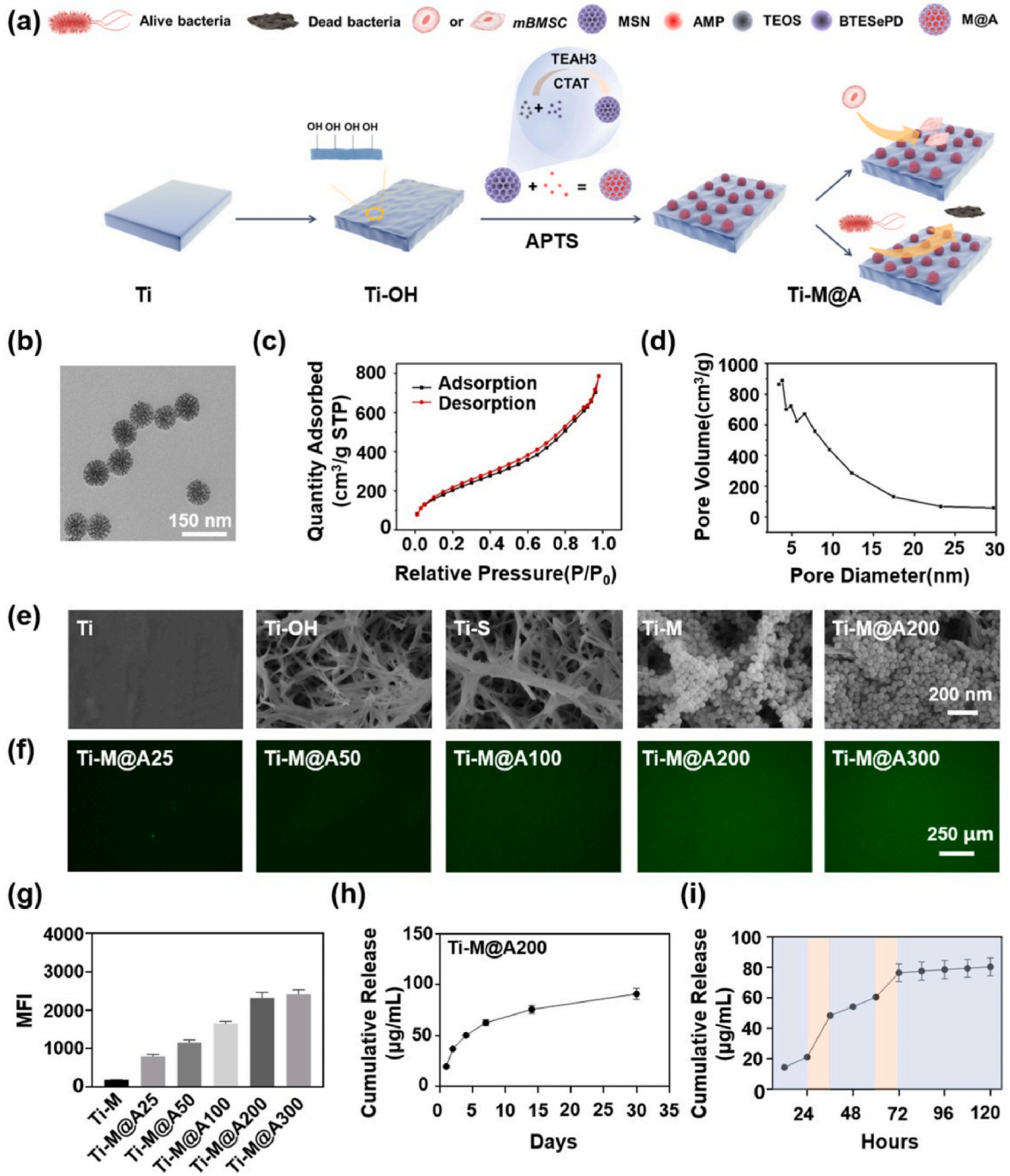

Fig. 1. Characterization of the functionalized titanium surfaces. (a) Schematic diagram showing the preparation process of the functionalized titanium implant. (b) TEM image of MSNs. (c) Nitrogen adsorption-desorption isotherms and (d) pore size distribution of MSNs. (e) SEM images and (f) fluorescent images of different functionalized surfaces. (g) The quantitative results of the mean fluorescent intensity (MFI) on the indicated surfaces. (h) The drug release curves of AMPs from Ti-M@A200 in PBS. (i) The drug release curves of AMPs from Ti-M@A200 in switched microenvironments between PBS and H_2O_2. The periods with blue color were in PBS, and those with orange color were in PBS containing 100 μM H_2O_2. (For interpretation of the references to color in this figure legend, the reader is referred to the Web version of this article.)

poor stability of the adsorbed AMP, and the burst release of such cationic peptides in the early stage may cause unwanted cytotoxicity. On the other hand, the covalent binding method is difficult to control the grafting efficiency, and the exposed AMPs on the surface are susceptible to enzymatic degradation [34]. Thus, controlled AMP delivery remains a challenge in titanium-based biomaterials. Therefore, the tailored design of sophisticated titanium surfaces should be able to realize the controllable and long-term activity of AMPs, thus achieving maximal antibacterial effects with minimal side effects.

Bioactive materials exhibit advantages in immune bioactivities by regulating cell behaviors and functions [35–37]. A common strategy to regulate osteogenic properties is to integrate bioactive factors with implants. Selenium (Se) is an essential element in the human body and plays regulatory roles in osteogenesis, inflammation and so on [38,39]. Se can protect stem cells from osteogenic differentiation inhibition and improve osteogenic activity by inhibiting oxidative stress [40]. Beyond regulating inflammation and osseointegration, Se-containing bioactive materials have been employed as redox-responsive carriers for the controlled delivery of biomolecules [41]. With these findings in mind, we hypothesized that the Se-assisted functionalization of titanium implants might integrate on-demand AMP release and regulation of inflammation and osseointegration for efficient and safe regenerative medicine applications.

In this study, we developed a bioactive titanium implant by anchoring the AMP of HHC36 and Se on the surface for their anti-infection, anti-inflammation and pro-osseointegration effects (Fig. 1a). First, we immobilized diselenide-bridged mesoporous silica nanoparticles (MSNs) as a carrier with HHC36 on a titanium surface through silica coupling agents. We investigated the antimicrobial activity of the functionalized implant against four clinical bacteria (*Staphylococcus aureus* (*S. aureus*), *Escherichia coli* (*E. coli*), *Pseudomonas aeruginosa* (*P. aeruginosa*) and *methicillin-resistant S. aureus* (*MRSA*)). Next, we evaluated the influence of the implant on the osteogenic activity to *mouse bone marrow-derived mesenchymal stem cells* (*mBMSCs*) and the polarization of *RAW 264.7* macrophages *in vitro*, along with the regenerative effect in a New Zealand rabbit bone defect model *in vivo*. Our study provides a proof of concept for the employment of bioactive functionalization to overcome bacterial infection and dysregulated inflammation for effective implant osseointegration.

2. Experimental section

2.1. Materials

Titanium (Ti) wafers (5 × 5 × 0.1 and 10 × 10 × 0.1 mm^3) and rods (φ 2 mm × 6 mm) were purchased from Chenhui Metal Ltd. (Baoji, China). The peptides were synthesized by Qiangyao Biotechnology Co., Ltd. (Shanghai, China). γ-Aminopropyl triethoxysilane (APTS) was purchased from Sigma–Aldrich. (Missouri, USA). Sodium hydroxide (NaOH) and ethanol were purchased from Guangdong Reagent Technology Co., Ltd. (Zhaoqing, China). Phosphate-buffered saline (PBS) was obtained from ThermoFisher Biochemical Products Co., Ltd. (Beijing, China). LB agar, nutrient broth and tryptic soy broth were purchased from Guangzhou Huankai Microbial Sci. & Tech. Co., Ltd. (Guangzhou, China). *Staphylococcus aureus* (*S. aureus*, ATCC 6538P), *Escherichia coli* (*E. coli*, ATCC 8739), *Pseudomonas aeruginosa* (*P. aeruginosa*, ATCC 15442) and *methicillin-resistant Staphylococcus aureus* (*MRSA*, ATCC 43300) were purchased from Guangdong Microbial Culture Collection Center (Guangzhou, China). Micro BCA assay kit, fetal bovine serum (FBS) and 0.25 % trypsin were obtained from ThermoFisher Biochemical Products Co., Ltd. (Beijing, China). BCA Protein Assay kit was purchased from Lead Biotech (Guangzhou, China). Alkaline phosphatase assay kit and DAPI were purchased from Beyotime Biotechnology Ltd. (Guangzhou, China). F-actin was purchased from AAT Bioquest (California, USA). Triton X-100 was purchased from Invitrogen (California, USA). Hexadecylpyridinium chloride was purchased from Sigma–Aldrich (St Louis, USA). Trizol reagent with RNA extract kit was purchased from Invitrogen (Carlsbad, USA). Reverse transcription kit and reverse/forward primers were purchased from TAKARA (Kyoto, Japan). Basal medium with L-glutamine (1 %) and penicillin/streptomycin (1 %), and *mouse bone marrow-derived mesenchymal stem cells* (*mBMSCs*) were purchased from Cyagen Ltd. (Guangzhou, China). Macrophages *RAW 264.7* cells were purchased from Yuanjing Biotechnology Ltd. (Guangzhou, China).

2.2. Preparation and characterization of MSN@AMP

The bis[3-(triethoxysilyl)propyl] diselenide (BTESePD) was synthesized as reported in our previous work [41–43]. The MSN nanoparticles were synthesized via a modified sol-gel method. First, 0.6 g of cetyltrimethylammonium tosylate (CTAT) was dissolved in 40 mL of water as the structure-directing agent. Then, 0.15 g of triethanolamine ($TEAH_3$) was used as the alkaline catalyst, and the solution was continuously stirred at 80 °C for 30 min. A mixture of 3.0 g tetraethyl orthosilicate (TEOS) and 2.0 g BTESePD was added dropwise to the above solution and stirred for another 4 h. The obtained MSNs were centrifuged, washed with ethanol, and refluxed in an ethanol solution of NH_4NO_3 to remove CTAT.

For AMP loading, the MSNs and AMPs were suspended in 95 % ethanol with different mass ratios of MSN to drug. The mixture was continuously shaken at 500 rpm for 24 h. The AMP-loaded MSNs (M@A) were washed and collected for further applications.

The loading content of AMP was analyzed by a Micro BCA assay [44]. In brief, the supernatant after centrifugation was treated with the working reagent of the Micro BCA assay kit (MA:MB:MC = 25:24:1). Then, the systems were incubated in the dark at 37 °C for 2 h. The absorbance of the incubation solution at 562 nm was measured by a microplate reader (Varioskan Flash, Thermo, USA). The supernatant concentration of the AMP was calculated according to a fitted standard curve. The loading capacity (LC) of MSN was calculated as follows:

LC % = (Total drug – supernatant content)/AMP loading MSN mass × 100 %

The morphologies of MSN nanoparticles were characterized by Transmission Electron Microscope (TEM, JEM-2100F, JEOL, Japan) and Scanning Electron Microscope (SEM, JSM6330F, JEOL, Japan). The hydrodynamic diameter and zeta potential of the MSNs and M@A in water were characterized by a Nano-ZS 90 Nanosizer (Malvern Instruments, Worcestershire, UK). The specific surface areas and pore size distributions were evaluated and calculated by the Brunauer–Emmett–Teller (BET) and Barrett–Joyner–Halenda (BJH) methods, measured by an automatic gas adsorption analyzer (Autosorb iQ, Anton Paconta Technology, USA). XPS assays were performed on a spectrometer (ThermoFisher ESCALAB Xi+) using an Al Kα (1486.4 eV and 650 μm spot size) radiation source. The analyzer pass energy was set at 100 eV for survey scans and at 40 eV for high-resolution scans.

2.3. Preparation and characterization of the functionalized titanium (Ti) surfaces

Ti wafers were cleaned by sonicating for 15 min in ethanol and 15 min in deionized water. To obtain hydroxyl-modified titanium (Ti–OH), Ti wafers were treated with 5 M NaOH solution at 60 °C for 24 h. The samples were washed with distilled water for 3 times and dried in nitrogen. For the preparation of functionalized Ti wafers, Ti–OH substrates were subsequently soaked in 95 % ethanol solution containing APTS (1 mg/mL), or 95 % ethanol solution containing APTS (1 mg/mL) and M or M@A with different concentrations (25, 50, 100, 200, 300 μg/mL) at 50 °C for 12 h. The functionalized samples were referred to as Ti–S, Ti-M and Ti-M@A, respectively.

FITC-tagged AMP was used to characterize the modification of M@A on the titanium surface. Different concentrations of FITC-tagged AMP (50, 100, 200, 400, 600 μg/mL) or M@A-FITC solutions (25, 50, 100,

200, 300 μg/mL) were used to construct the functionalized surfaces (Ti-A or Ti-M@A). Then, the fluorescence distribution and average fluorescence intensity (MFI) on the surfaces were observed by a fluorescence microscope (DFC550, Leica, Germany). For the drug release analysis, Ti-M@A with FITC-tagged AMP ($10 \times 10 \times 0.1$ mm^3) was soaked in 500 μL of PBS and gently shaken at 100 rpm at 37 °C. At the indicated times, the amount of released AMP in the supernatant was analyzed based on the fluorescence intensity of FITC measured by a microplate reader (Varioskan Flash, Thermo, USA).

To characterize the stability of MSN and M@A on the titanium surfaces, Ti-M and Ti-M@A ($10 \times 10 \times 0.1$ mm^3) were immersed in 300 μL PBS buffer and gently shaken at 37 °C. The PBS buffer was changed every 7 days, and the samples were removed at the indicated times and dried. The change in surface morphology was observed by SEM (JSM6330F, JEOL, Japan).

For the mechanical stability assay, Ti rods (φ 2 mm × 6 mm) were used to prepare the functionalized Ti-M and Ti-M@A implants. Then, two holes (φ 3 mm) were drilled into the freshly harvested rabbit femurs. Additionally, Ti screws (φ 2.8 mm) were used to prepare the functionalized Ti-M, and the holes (φ 2.3 mm) were drilled into the freshly harvested pig femurs. After repeated insertion and extraction of the implants, the morphology of the surface was observed by SEM (JSM6330F, JEOL, Japan).

2.4. In vitro antimicrobial assay

Bacteria were plated on agar plates and cultured overnight. Then, a single bacterial colony was incubated in broth culture medium for 6 h at 37 °C at 220 rpm. After that, the bacterial suspension was counted by the spectrophotometer method and diluted with PBS to obtain the indicated concentration.

For the agar plate test, the surfaces ($5 \times 5 \times 0.1$ mm^3) were independently placed into 48-well plates. Then, 10 μL of bacterial suspension (1×10^6 CFU/mL) was dropped on each implant surface. After 2 h of culture at 37 °C, the implants were independently transferred into 2-mL Eppendorf tubes. Then, 990 μL PBS was added, and the system was vortexed thoroughly. After that, 10 μL of diluted bacterial solution was dropped on agar plates and spread over, followed by CFU colony counting after overnight incubation at 37 °C.

For the scanning electron microscopy (SEM) assay, the surfaces ($5 \times 5 \times 0.1$ mm^3) were placed into 48-well plates independently. Then, 10 μL of *S. aureus* suspension or *E. coli* suspension (1×10^8 CFU/mL) in PBS was dropped onto the implants and cultured at 37 °C for 2 h. Then, paraformaldehyde solution (4 %) was added to fix the bacteria at 4 °C for 12 h, and gradient dehydration was performed with ethanol from 30 % to 100 %. The samples were coated with gold for the SEM assay (JSM6330F, JEOL, Japan).

For the antibiofilm assay, bacterial suspensions were centrifuged and resuspended in TSB medium (1×10^8 CFU/mL). Then, 10 μL of the bacterial suspension was placed on the implants ($10 \times 10 \times 0.1$ mm^3), followed by the addition of 990 μL of TSB medium. The system was cultured for 36 h at 37 °C. After 24 h of culture, the culture medium was replaced. Then, the medium was extracted gently, and the implants were washed carefully with PBS. Subsequently, the implants were stained with 250 μL of crystal violet solution for 30 min in the dark and cleaned carefully with PBS buffer. The formation of biofilms was photographed by a digital fluorescence microscope (DFC550, Leica, Germany) under a bright field. After that, we used ethanol to dissolve the crystal violet of the biofilm, and the absorbance was determined by an ELISA reader (TECAN Infinite M200 PRO, Switzerland) at 590 nm.

2.5. In vitro cell assay

The *mBMSCs* were cultured in mesenchymal stem cell growth medium at 37 °C in a 5 % CO_2 incubator. *RAW 264.7* cells were cultured in DMEM containing fetal bovine serum (10 %) at 37 °C in a 5 % CO_2 incubator. The medium was replaced every 3 days, and cells at passages 3–5 were used for the experiments.

For the CCK-8 assay, the implants ($5 \times 5 \times 0.1$ mm^3) were incubated with *mBMSCs* or *RAW 264.7* cells for the indicated times. Then, the implants were moved to a new 48-well plate, and 250 μL of culture medium containing 10 % CCK-8 solution was added. After 2 h of incubation at 37 °C in the dark, 100 μL of the solution was transferred to a 96-well plate, and the absorbance was determined by an ELISA reader (TECAN Infinite M200 PRO, Switzerland) at 450 nm.

For the cell morphology assay, the implants ($10 \times 10 \times 0.1$ mm^3) were cultured with *mBMSCs* or *RAW 264.7* cells for the indicated times and incubated with paraformaldehyde at 4 °C for 1 h. Then, 0.1 % Triton-PBS solution was added to permeabilize the cells for 10 min. Next, the cells were stained with F-actin for 1 h in the dark and DAPI for 8 min in the dark. The implants were washed with PBS before each step. The cell morphology was observed by confocal laser scanning microscopy (CLSM) (Leica TCS SP5, Germany).

For the Alizarin red staining assay, the implants ($10 \times 10 \times 0.1$ mm^3) were cultured with *mBMSCs* (5×10^4 cells). After 24 h of incubation, the culture medium was changed to osteogenic induction medium containing 10^{-5} mM dexamethasone, 50 μM ascorbic acid and 10 mM sodium β-glycerophosphate. At the indicated times, the implants were moved to a new 24-well plate and washed with PBS. The cells on the implants were stained with alizarin red for 15 min in the dark. Then, the implants were washed with distilled water to eliminate excess staining. The precipitates were observed by stereo microscopy (Zeiss SteREO Discovery. V12, ZEISS). Finally, the precipitates were dissolved in 10 % cetylpyridinium chloride and quantified by an ELISA reader (TECAN Infinite M200 PRO, Switzerland) at 562 nm.

To assay alkaline phosphatase (ALP) activity, the implants ($10 \times 10 \times 0.1$ mm^3) were cultured with *mBMSCs* (5×10^4 cells). After 24 h of incubation, the culture medium was changed to osteogenic induction medium. At the indicated times, the implants were moved to a new 24-well plate. Then, the implants were washed with PBS and immersed in 350 μL of Western and IP cell lysate (without inhibitor) at 4 °C for 2 h. The lysate was collected and centrifuged for 3 min at 12000 rpm at 4 °C, and the supernatant was collected for ALP activity detection. The ALP Activity Assay Kit was used to analyze the ALP activity, and the BCA Protein Assay Kit was used to detect the protein content.

For the quantitative real-time polymerase chain reaction (qRT-PCR) assay, the implants ($10 \times 10 \times 0.1$ mm^3) were cultured with *mBMSCs* (5×10^4 cells). After 24 h of incubation, the culture medium was changed to osteogenic induction medium. At the indicated times, total RNA was extracted using TRIzol reagent with an RNA extraction kit. RNA reverse transcription was performed using the Prime Script TMRT reagent kit. qRT-PCR was performed using a real-time fluorescence quantitative PCR instrument (QuantStudio 6 Flex, Life Technologies, USA) under two-step cycling conditions. The PCR primer sequences are presented in Table S1.

RAW 264.7 macrophages were used to evaluate anti-inflammatory activity *in vitro*. The implants ($10 \times 10 \times 0.1$ mm^3) were cultured with *RAW 264.7* (3×10^4 cells) for 3 days. Then, the cells were treated with/without LPS (40 ng/mL)-containing media to stimulate macrophage polarization. After culture for another 24 h, the anti-inflammatory activities were evaluated.

qRT−PCR was used to evaluate the expression levels of representative proinflammatory genes of the M1 type (TNF-α, iNOS) and anti-inflammatory genes of the M2 type (IL-1ra and CD206) in *RAW 264.7* after different treatments. The PCR primer sequences are presented in Table S2.

To assess macrophage polarization, characteristic surface biomarkers of M1-type macrophages (CD86) and M2-type macrophages (CD206) on different substrates were assayed by flow cytometry (Beijing Challen Biotechnology Co., Ltd, FongCyte). Macrophages were transferred into 24-well plates and rinsed with PBS. After that, the cells were collected with a cell scraper and rinsed with blocking buffer for 20 min at 4 °C. Then, the cells were washed and stained for BV510 CD11b, APC

CD86 (M1 marker) and FITC CD206 (M2 marker). Finally, macrophage polarization was quantified by using a flow cytometer and analyzed by using FlowJo software.

2.6. In vivo study

The *in vivo* experiments were approved by the Medical Laboratory Animal Center of Guangdong Province (Foshan, China). New Zealand white rabbits (10–12 weeks, 2.0–2.5 kg) were used (18 for the infection model, 12 for the non-infection model). The rabbits were anesthetized, and two holes (φ 3 mm) were drilled in each of the two femurs. For the infection model, the samples (φ 2 mm × 6 mm) were implanted with the *S. aureus* suspension (1×10^8 CFU/mL, 15 μL). For the non-infection model, the samples were implanted without bacteria. The soft tissues were closed, and the skin was sutured. Ti, Ti-M and Ti-M@A implants were employed for the *in vivo* assay.

For the antimicrobial assay, after 7 and 60 days of implantation, the rabbits were sacrificed. The implants were collected, immersed in nutrient broth medium, and shaken for 4 h at 120 rpm/min at 37 °C. Then, the bacterial suspensions were collected to evaluate the bacterial viability by blood agar plates.

For hematoxylin and eosin (H&E) staining, at the indicated times after implantation, the femurs without implants were collected and immersed in 4 % paraformaldehyde for 3 d and in ethylenediaminetetraacetic acid (EDTA) for 45 d, followed by dehydration with a gradient of ethanol solutions (50 %, 70 %, 80 %, 95 % and 100 %) for 2 h, 2 h, 1.5 h, 1 h (twice) and 45 min (twice). The tissues were placed in dimethylbenzene for 30 min and embedded in paraffin wax for 2 h at 60 °C. After cooling for solidification, 4 μm sections were acquired. For H&E staining of the anti-infection assay, the sections were treated with hematoxylin for 2 min and eosin solution for 5 min. The sections were observed by a Pannoramic Scanner (3DHISTECH, Pannoramic P250FLSAH).

For methylene blue & basic fuchsin staining, after the indicated implantation period, the femurs with implants were collected and fixed in 10 % formalin and dehydrated 8 times with acetone at −20 °C. Then, the tissues were embedded in polymethylmethacrylate (PMMA), eroded with 2 % hydrochloric ethanol for 1 min and washed with distilled water. After that, the tissues were immersed in methylene blue for 1 min and basic fuchsin for 1 min. Finally, the tissues were cut into 10–20 μm sections with a microtome (SAT-001, AoLiJing, China) and observed by digital fluorescence microscopy (Leica, DM6M).

For micro-CT analysis, the femurs with implants were fixed in 4 % paraformaldehyde for 72 h and immersed in 75 % ethanol. Then, the samples were scanned with a μCT-100 micro-CT scanner (SCANCO Medical AG, Switzerland). The bone-to-implant contact (BIC), the bone volume per total volume (BV/TV) and the trabecular thickness (Tb.Th) were calculated.

2.7. Statistical analysis

The experiments used at least 3 parallel samples, and the results are shown as the means ± standard deviations. Statistical significance was calculated by Origin 8.0 using the *t*-test method. The confidence levels were set as * ($p < 0.05$), ** ($p < 0.01$) and *** ($p < 0.001$).

3. Results

3.1. Synthesis and characterization of the functionalized titanium implants

Diselenide-bridged MSNs were prepared according to our previous reports. The TEM images showed that the diselenide-bridged MSNs had a uniform spherical morphology with an average diameter of approximately 50 nm (Fig. 1b) and possessed an obvious mesoporous structure. The N_2 adsorption-desorption isotherm showed a typical type IV curve and well-defined pore sizes (centered at 12.7 nm). Based on the BJH model, the surface area and total pore volume of MSNs were 490.83 m^2/g and 1.025 cm^3/g, respectively (Fig. 1c and d). The loading capacities of the AMP HHC36 were 280.8, 379.2 and 409.3 μg/mg with mass ratios of MSN to AMP mass ratios of 1:1, 1:2 and 1:3, respectively. Considering the drug loading capacity and efficiency, the optimal drug-carrier mass ratio was determined to be 1:2 for subsequent experiments with a loading efficiency of 27.5 %; and this sample was referred to as M@A. Additionally, the zeta potential of M@A (−12.1 mV) was lower than that of pristine MSNs (−26.9 mV), further confirming the successful absorption of the positively charged peptide (Fig. S1).

The smooth pristine Ti substrates after alkali treatment were oxidized to form hydroxyl-modified Ti substrates (Ti–OH) with rough network microstructures on the surface (Fig. 1e and Fig. S2). Then, APTS was further used as a crosslinking reagent to anchor the MSNs or M@A on the Ti–OH substrate to prepare Ti-M and Ti-M@A, respectively. The scanning electron microscopy (SEM) images showed that the rough network microstructures of the substrate enabled the MSNs and M@A to anchor abundantly onto the Ti–OH surface on Ti-M and Ti-M@A200, respectively (Fig. 1e and Fig. S2). The fluorescence assay results with the FITC-labeled AMP showed that the content of the anchored M@A increased as the feeding concentration of M@A increased from 25 μg/mL (Ti-M@A25) to 300 μg/mL (Ti-M@A300), demonstrating that the density of the nanoparticles on Ti–OH was concentration dependent (Fig. 1f and g). Moreover, the MFI of Ti-M@A200 (2319.65. a.u.) was similar to that of Ti-M@A300 (2414.97. a.u.) (Fig. 1g). Considering the comparable MFI and corresponding amounts of AMP loaded on Ti-M@A200 and Ti-M@A300, we selected Ti-M@A200 (denoted Ti-M@A) for subsequent experiments. Additionally, to characterize the non-specific adsorption of AMP molecules on the surface, we used FITC-tagged AMP instead of M@A for testing. The results (Fig. S3) showed that the increase of the surface fluorescence was very limited after reacting with the fluorescent peptide, with the MFI of only 423.07 a.u. for the surface obtained with AMP concentration of 600 μg/mL. This value was much lower than that of Ti-M@A200 and Ti-M@A300, indicating that the non-specific adsorption of AMP on the surface could be considered negligible.

Moreover, the weakened Ti peak and enhanced Si peak of Ti-M@A in the XPS spectrum indicated the successful immobilization of M@A on the substrate (Fig. S4). The divided C═O peak in the high-resolution C1s spectrum indicated that the AMP in the MSNs was stable during the immobilization process (Fig. S4).

The release properties of the AMP from Ti-M@A were further characterized. Ti-M@A showed a slow and sustainable release of the AMP for 30 days under physiological conditions, which might reduce the adverse effects of antimicrobial peptide leakage on osseointegration (Fig. 1h). According to previous researchers [45], acute and long-term bacterial infection will induce a redox microenvironment with an increased H_2O_2 concentration. We therefore used PBS containing 100 μM H_2O_2 to simulate the microenvironment of bacterial infection and studied the release profiles of the AMP from Ti-M@A in this switched microenvironment. The slow release of the AMP changed to burst release from Ti-M@A in the presence of H_2O_2 and then returned to normal conditions, highlighting the achievement of effective bacterial infection-responsive AMP release (Fig. 1i). These results demonstrated that Ti-M@A could sustainably release the AMP in response to the microenvironment of bacterial infection.

The long-term stability of the functionalized surfaces was also characterized. The SEM results showed that the morphologies and amount of MSNs on Ti-M and Ti-M@A had slight decrease after 30 days of degradation (Fig. 2a and b), and the vast majority of the nanoparticles were immobilized evenly on the substrates. We also characterized the mechanical stability of the implant by simulating possible mechanical damage during surgery (Fig. 2c to e, Fig. S5). After mechanical insertion and removal, the surface had negligible changes and still showed an even distribution of abundant nanoparticles. These results demonstrated

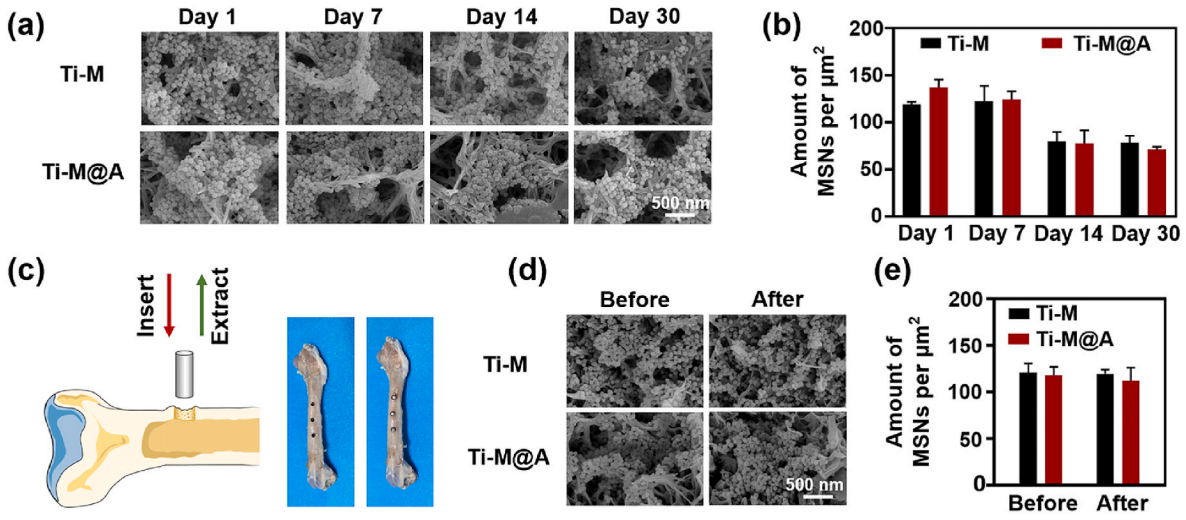

Fig. 2. Stability of the functionalized titanium surface. (a) SEM images of the surfaces and (b) the amount of MSNs on the surfaces after being immersed in PBS for 1, 7, 14 and 30 days (n = 3). (c) Schematic and images of the mechanical stability experiments. (d) SEM images of the implant surfaces and (e) the amount of MSN on the surfaces before and after insertion into the femur (n = 3).

that MSN-assisted interfacial functionalization on the titanium surface had excellent degradation and mechanical friction stability, meeting the requirements for further application.

3.2. *In vitro antimicrobial activities*

The antimicrobial activities of Ti-M@A against four types of bacteria, including *S. aureus*, *E. coli*, *P. aeruginos* and *MRSA*, were investigated *in vitro*. The implant had no observable bactericidal ability without AMP (Ti, Ti–OH, Ti–S and Ti-M), while the bactericidal performance was positively correlated with the concentration of M@A (Fig. 3a). Notably, due to the similar content of anchored M@A, both Ti-M@A (Ti-M@A200) and Ti-M@A300 showed strong, broad-spectrum antimicrobial activity, killing 98.02 % and 98.13 % of *S. aureus*, 98.50 % and 98.39 % of *E. coli*, 96.87 % and 96.50 % of *P. aeruginosa*, and 95.71 % and 96.04 % of *MRSA*, respectively. The antibacterial mechanism was then explored. The SEM images showed that the *S. aureus* and *E. coli* adhered to the Ti, Ti–OH, Ti–S and Ti-M substrates maintained intact cell walls and integrated membranes (Fig. 3b). Conversely, membrane shrinkage and severe cytoplasm leakage from the *S. aureus* and *E. coli* adhered to Ti-M@A were observed, recovering the antibacterial mechanism by destroying their membrane (Fig. 3b). Bacteria can attach to the surface of the implant and form biofilms, leading to bacterial infection and preventing osseointegration [46,47]. Therefore, the inhibitory ability against biofilms was further evaluated by a crystal violet staining assay. Compared to the Ti, Ti–OH, Ti–S and Ti-M groups, the negligible violet staining on the Ti-M@A surface indicated effective inhibition of biofilm formation, being consistent with the antimicrobial activity results (Fig. 3c). Quantitative analysis further demonstrated that the biofilms of *S. aureus*, *E. coli*, *P. aeruginosa* and *MRSA* on Ti-M@A were significantly decreased to 21.99 %, 50.33 %, 25.68 % and 44.40 %, respectively, compared to those on pristine Ti (Fig. 3d). These results together demonstrated that Ti-M@A exhibited excellent antibacterial and anti-biofilm activities.

3.3. *In vitro biocompatibility, osteogenic activity and anti-inflammatory activity*

Since biocompatibility is an inevitable concern with implants in tissue engineering, the cytotoxicity of the functional substrate to *mBMSCs*, one of the main cell types involved in osseointegration, was evaluated by CCK-8 assay (Fig. 4a and Fig. S6). The results showed that all implants exhibited negligible cytotoxicity to the cells. After 1, 3 and 5 days of culture, cell viability on Ti-M@A was comparable to that on the Ti substrate. The cytoskeleton and nuclei of the cells were observed by CLSM by co-staining with F-actin and DAPI, and the results showed no significant difference in the number or morphology of the cells on all implants even after 5 days of culture (Fig. 4b). These results demonstrated that the functionalized surfaces exhibited excellent biocompatibility with negligible influence on the adhesion, spread and proliferation of *mBMSCs*.

We further evaluated the osteogenic activities of the functionalized substrates with *mBMSCs*. The alkaline phosphatase (ALP) quantitative results at 7 and 14 days showed that the *mBMSCs* on Ti-M and Ti-M@A displayed 1.22- and 1.22-fold (7 days) and 1.25- and 1.28-fold (14 days) higher levels of ALP activity than those on the pristine Ti, respectively, demonstrating the enhanced osteogenesis of *mBMSCs* (Fig. 4c). Furthermore, we found that this promoting effect was caused by the presence of Se in MSN, as the osteogenic activity of Ti-M(Se-) to *mBMSCs* disappeared when the Se element was removed, especially after 14 days of culture (Fig. S7). Meanwhile, after 7 and 14 days of culture, the calcium deposition of *mBMSCs* was 2.85- and 2.69-fold (7 days); and 1.52- and 1.45-fold (14 days) higher on Ti-M and Ti-M@A than that of the pristine Ti via ARS assay, respectively, demonstrating that the MSN-assisted interfacial functionalization promoted the differentiation of stem cells into osteoblasts (Fig. 4d and **e**). The improved osteogenic differentiation of *mBMSCs* on the functionalized surfaces was also characterized by qRT−PCR (Fig. 4f and **g**). After 7 days of culture, the expression levels of the osteogenic-related genes RUNX2 and OPN were significantly upregulated on Ti-M and Ti-M@A compared with those on the Ti substrate (Fig. 4f). After 14 days of culture, the expression level of the RUNX2 gene decreased, while the expression levels of the OCN and OPN genes were consistently higher than those in the Ti group (Fig. 4g).

Given that macrophages play crucial roles in the dynamic process of bone repair, we characterized the polarization of macrophages on the functionalized surfaces. After 1, 3 and 5 days of culture, MSN-assisted interfacial functionalization on the implant surfaces did not impact the viability or morphology of *RAW 264.7* cells (Fig. 5a and **b**). Moreover, macrophage polarization was analyzed by qRT−PCR. After 3 days of culture, and compared to the Ti group, the expression of proinflammatory cytokines and M1 marker genes (iNOS and IL-1β) in the Ti-M and Ti-M@A groups was prominently down-regulated (Fig. 5c to **d**). In contrast, the expression of anti-inflammatory cytokines and M2 marker genes (ArgI and CD206) was up-regulated (Fig. 5e to f). Consistently, flow cytometry analysis showed that the -*RAW 264.7* stimulated with LPS on Ti-M and Ti-M@A showed not only decreased

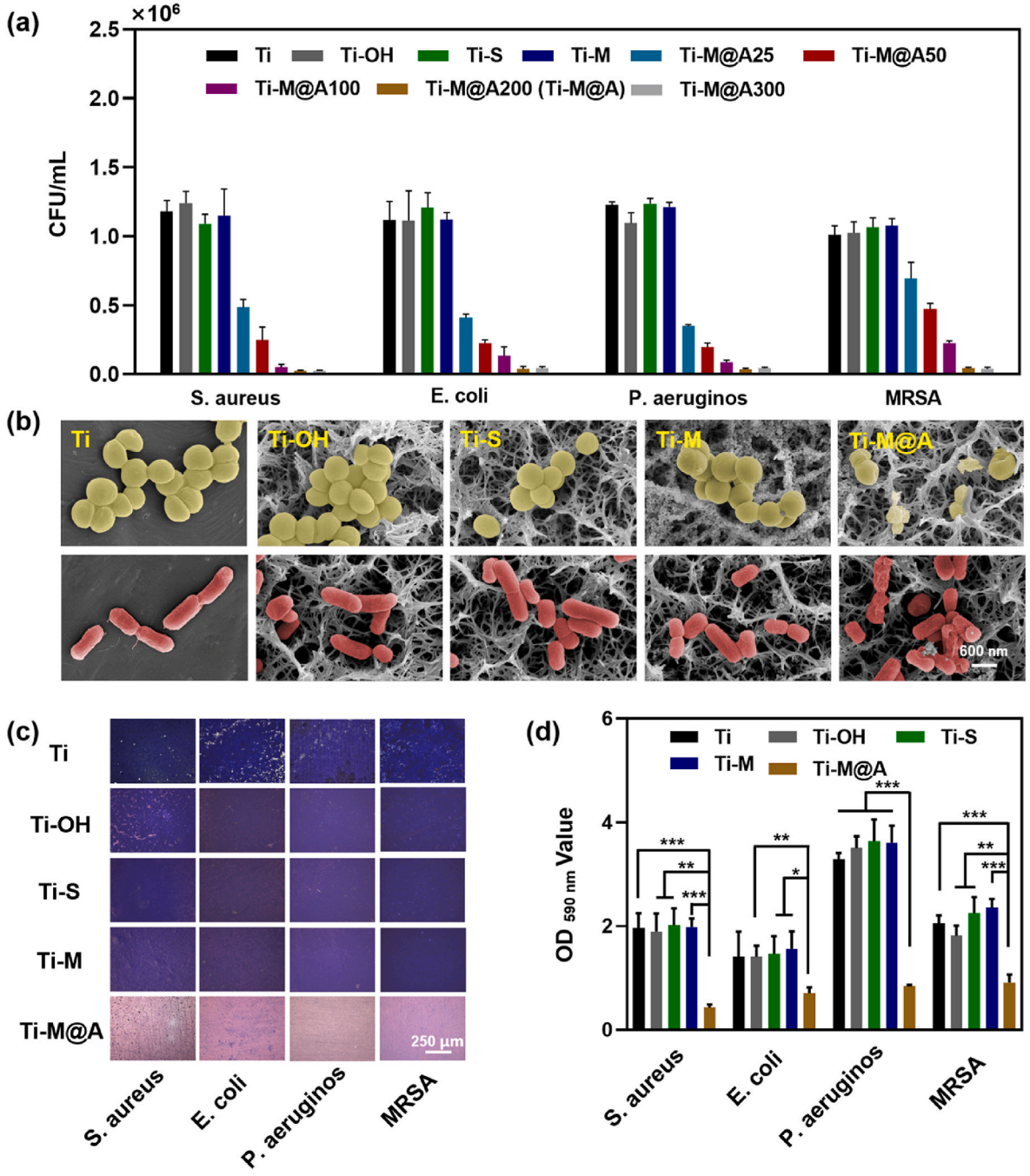

Fig. 3. *In vitro* antimicrobial activities of the functionalized titanium surfaces. (a) The antimicrobial activities of the functionalized surfaces against *S. aureus*, *E. coli*, *P. aeruginosa* and *MRSA* determined by the agar plate method (n = 3). (b) SEM images of *S. aureus* and *E. coli* on the surfaces after 2 h of culture. *S. aureus* is shown with a yellow false color, and *E. coli* is shown with a red false color. (c) Biofilm crystal violet staining of the indicated bacteria on the functionalized surfaces. (d) Quantitative analysis of biofilm crystal violet staining (n = 3) * denotes $p < 0.05$, ** denotes $p < 0.01$, *** denotes $p < 0.001$. (For interpretation of the references to color in this figure legend, the reader is referred to the Web version of this article.)

CD86-positive populations (M1 marker) (Fig. 5g and Fig. S8) but also increased CD206 populations(M2 marker) (Fig. 5h and Fig. S9). ROS play an important role in the process of inflammation and macrophage polarization [48]. We thus quantitatively studied the ROS content in macrophages and found that MSN-assisted interfacial functionalization on implant surfaces effectively scavenged ROS in LPS-activated macrophages (Fig. 5i and Fig. S10), which was expected to promote the reprogramming of macrophages to the M2 phenotype [38,49].

3.4. *In vivo* bone regeneration in bone defect/non-infection model

Osseointegration at the bone-implant interface is crucial for the successful application of implants; thus, an *in situ* bone defect model was used to characterize osseointegration (Fig. 6a). After implantation for 7 days, the macrophage phenotype at the bone-implant interface was analyzed by IHC staining for iNOS in M1 macrophages and CD206 in M2 macrophages. The results (Fig. 6b) showed that a negligible iNOS-positive population was observed on the Ti-M and Ti-M@A implants compared with the pristine Ti implants. In contrast, a larger CD206-positive population was observed. As reported, in the initial stage,

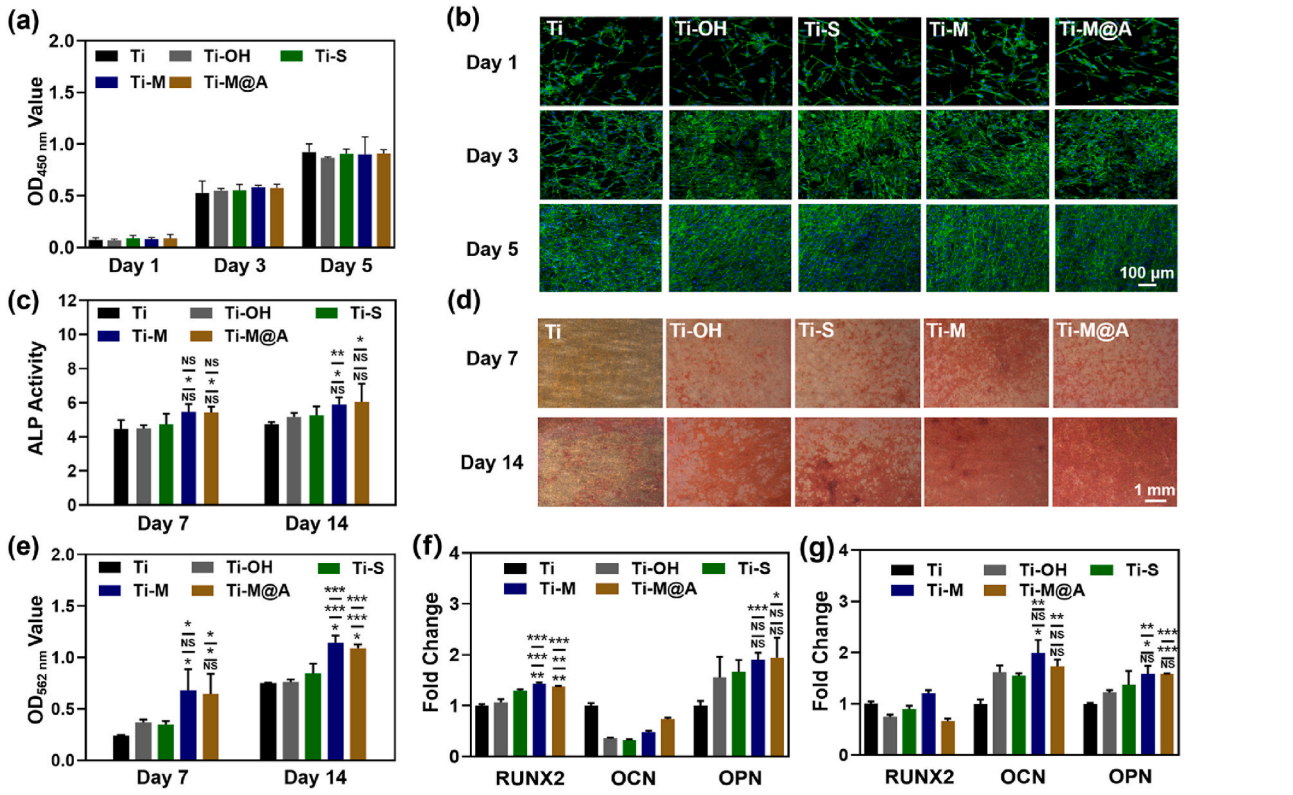

Fig. 4. Biocompatibility and osteogenic activities of the functionalized titanium surfaces. (a) CCK-8 results for the indicated surfaces with *mBMSCs* after 1, 3 and 5 days of culture (n = 3). (b) The morphology of *mBMSCs* on the indicated surfaces after 1, 3 and 5 days of culture. The cell nuclei were stained blue with DAPI, and the cytoskeletons were stained green with F-actin. (c) The ALP activity of *mBMSCs* on the indicated surfaces after 7 and 14 days of culture (n = 3). (d) Alizarin red S staining images and (e) the absorbance values at 562 nm after 7 and 14 days of culture (n = 3). The expression of osteogenic genes in *mBMSCs* on the indicated surfaces after (f) 7 and (g) 14 days of culture (n = 3). In (c), (e), (f) and (g), * denotes $p < 0.05$, ** denotes $p < 0.01$, and *** denotes $p < 0.001$. The three lines of significant differences were compared to Ti, Ti–OH and Ti–S, respectively, from top to bottom. (For interpretation of the references to color in this figure legend, the reader is referred to the Web version of this article.)

macrophages can polarize towards the proinflammatory M1 type for immune activation and then transform towards the anti-inflammatory M2 phenotype to participate in bone repair. However, the abnormal proinflammatory microenvironment at the bone–implant interface severely hinders osseointegration [50,51]. Therefore, the above results demonstrated that MSN-assisted interfacial functionalization on implants could facilitate macrophage polarization towards the M2 phenotype for osseointegration *in vivo*.

After 60 days of implantation, methylene blue and basic fuchsin, as well as toluidine blue staining were conducted to evaluate osseointegration (Fig. 6c and **d**). The pristine Ti implants showed insufficient osseointegration at the bone–implant interface and the appearance of fibrous connective tissue. In contrast, MSN-assisted interfacial functionalization on Ti-M and Ti-M@A showed tight bonding to the tissues, highlighting adequate osseointegration. Then, we quantitatively analyzed the percentage of osseointegration in the region of interest (Fig. 6e). The improvements in the percentage of osseointegration were detected on the Ti-M and Ti-M@A implants compared to the pristine Ti implants, as evidenced by the higher bone-implant interface (BIC) and lower fibrous connective tissue area (Fig. 6f and **g**). From the corresponding Micro-CT images, we observed obviously increased bone volume per total volume (BV/TV), trabecular thickness (Tb.Th) and BIC (Fig. 6h–j and S11). The above results demonstrated that MSN-assisted interfacial functionalization on the Ti-M and Ti-M@A implants significantly promoted osseointegration *in vivo*.

3.5. *In vivo antibiosis, anti-inflammation and bone regeneration in the bone defect/infection model*

We further employed an implant-associated infection model in New Zealand rabbits to verify the antibacterial and anti-inflammatory activities of the implant at the interface to facilitate osseointegration *in vivo*. As depicted in Fig. 7a, the implant was inserted into the defect on the femur with *S. aureus* (10^8 CFU/mL, 15 μL). After 7 and 60 days of implantation, the implants with the marrow around them were removed to evaluate bacterial infection *in vivo* via the spread plate method. The results showed that there were severe bacterial infections in the Ti and Ti-M groups, but the Ti-M@A groups significantly reduced the amount of bacteria, killing 98.82 % of *S. aureus* after 7 days and 99.66 % after 60 days (Fig. 7b–c). These results revealed that MSN-assisted interfacial functionalization on Ti-M@A could enable the release of AMP to efficiently inhibit infection.

Bacterial infection at implant sites triggers surrounding soft tissue inflammation. After 7 and 14 days of implantation, H&E staining showed that Ti and Ti-M implants were surrounded by a larger number of inflammatory cells (Fig. 7d–f). In contrast, the inflammatory cell infiltration around Ti-M@A was only 20.61 % and 18.93 % compared to that around Ti at 7 and 60 days after implantation, respectively (Fig. 7d–f). Consequently, we further investigated whether the Ti-M@A implant could positively drive the functional reconstruction of macrophages. The population of iNOS-positive macrophages was markedly reduced, whereas the population of CD206-positive macrophages increased around Ti-M@A (Fig. 7g). These results verified that the Ti-M@A implants showed sufficient antibiosis and anti-inflammatory ability *in vivo*.

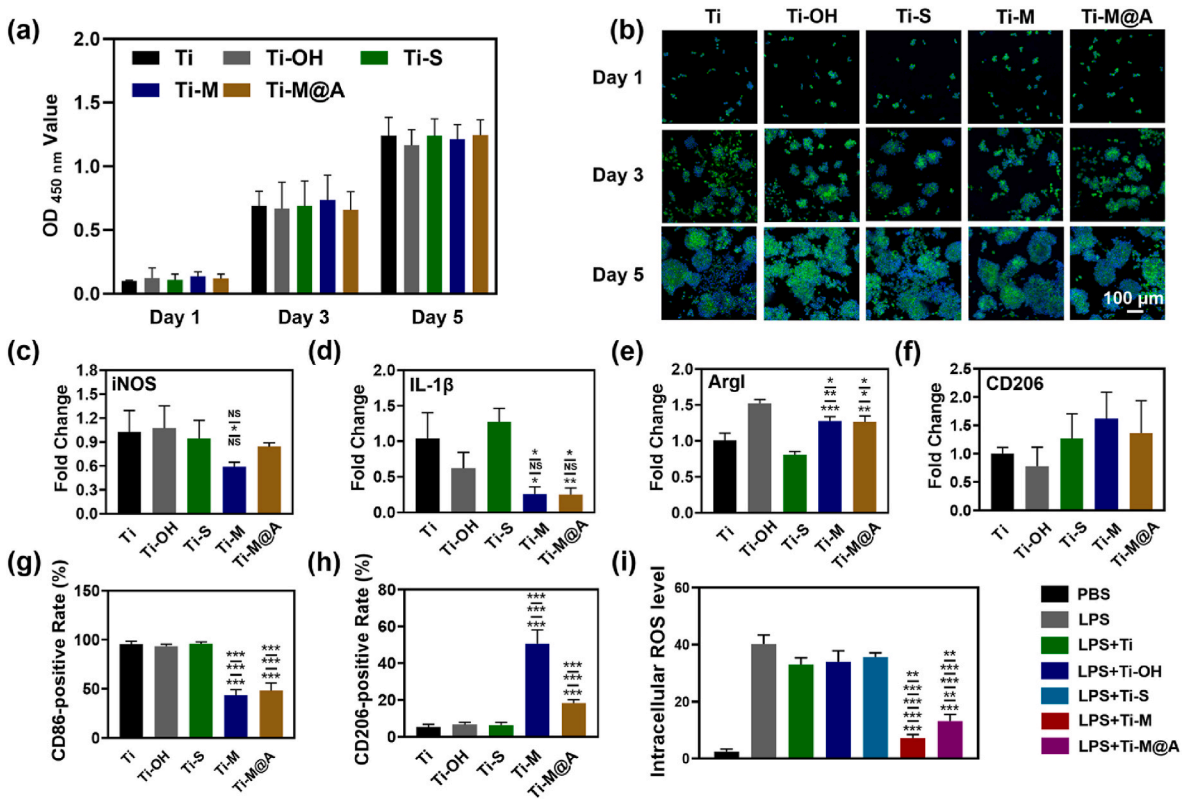

Fig. 5. Anti-inflammatory ability of the functionalized titanium surfaces. (a) CCK-8 results for the indicated surfaces with *RAW 264.7 cells* after 1, 3 and 5 days of culture (n = 3). (b) The morphology of *RAW 264.7* cells on the indicated surfaces after 1, 3 and 5 days of culture. The expression of the proinflammatory genes (c) iNOS and (d) IL-1β and the anti-inflammatory genes (e) ArgI and (f) CD206 in *RAW 264.7* cells after 3 days of culture on the indicated surfaces quantified by qRT–PCR assay (n = 3). (g) Quantitative analysis of the anti-inflammatory membrane protein CD206 by flow cytometry analysis after 3 days of culture (n = 3). (h) Quantitative analysis of the proinflammatory membrane protein CD86 by flow cytometry analysis after 3 days of culture (n = 3). (i) Quantitative analysis of intracellular ROS levels after various treatments (n = 5). * denotes $p < 0.05$. Cells were stained with DCFH-DA. In (c) to (i), * denotes $p < 0.05$, ** denotes $p < 0.01$, and *** denotes $p < 0.001$. The three lines of significant differences in (c) to (h) were compared to Ti, Ti–OH and Ti–S, respectively, from top to bottom. The five lines of significant differences in (i) were compared to PBS, LPS, LPS + Ti, LPS + Ti–OH and LPS + Ti–S, respectively, from top to bottom.

Accelerated osseointegration was observed around Ti-M@A. Methylene blue and basic fuchsin staining and subsequent quantitative analysis demonstrated that the BIC increased, but the area of fibrous connective tissues decreased in the Ti-M@A group (Fig. 7h–j). The Micro-CT results also verified the excellent osseointegration around Ti-M@A, as evidenced by the elevated BV/TV, Tb.Th and BIC values (Fig. 7k–m and Fig. S12). The above results showed that in the bone defect and infection model, the Ti-M@A implants could effectively inhibit infection and inflammation while simultaneously promoting osseointegration.

We also demonstrated that the peptide-loaded system had a broad spectrum of applications with other peptides, *e.g.*, YGFGG (Figs. S13–S19). The method by which Ti-M@Y was prepared was similar to that of Ti-M@A. We demonstrated the successful immobilization of YGFGG on the implant surface for release over a long period of time. Similarly, the Ti-M@Y surface exhibited excellent long-term stability and mechanical stability, which are conducive to the long-term promotion of osseointegration after implantation. We proved that Ti-M@Y had good biocompatibility, osteogenic and anti-inflammatory properties *in vitro*. In the bone defect/non-infection model, Ti-M@Y implants could significantly promote osteogenesis *in vivo*. The above results demonstrated the broad application prospects of our peptide-loaded system, which could enable the development of multifunctional implant surfaces to meet clinical needs.

4. Discussion

Bacterial infection and poor osseointegration around titanium implants can result in surgical failure and seriously threaten the health of patients [5]. Considering these two problems, dual-functionalized implants are in high demand. However, it is extremely difficult to achieve antibacterial and osseointegration properties simultaneously [13]. There have been numerous reports on the use of antimicrobial peptides (AMPs) for the surface of titanium implants [52,53], as well as the use of mesoporous silica nanoparticles (MSN) for loading and controlled release of AMPs [54–56]. However, there are few studies that combine the two.

In this study, driven by the urgent need for antimicrobial and osteogenic activities on the titanium implants, we loaded AMPs into MSN with osteogenic activity, and further constructed these nanoparticles on the titanium surface to achieve controlled release of AMPs and effective antimicrobial activity, as well as improved osteogenic activity of the implant. After implantation, bacterial adhesion and osteoblast-related cell adhesion occur on the implant surface at the same time with a competitive relationship. The key to the success of early implantation is the rapid osteogenic differentiation of cells and the prevention of bacterial infection on the implant surface [57]. Therefore, our system is expected to play an important role in the early osseointegration process.

S.aureus, *E. coli*, *P. aeruginosa* and *MRSA* have been identified as the most common microorganisms associated with implant infection and osteomyelitis, which can have serious consequences, including surgical failure, disability, sepsis and even patient death [58]. On the functionalized surfaces, AMPs released from MSNs provide excellent antimicrobial activity, efficiently inhibiting the growth of these four types of clinical bacteria. Additionally, in the clinic, it is important to prevent the formation of bacterial biofilms, as most clinical infections are related to

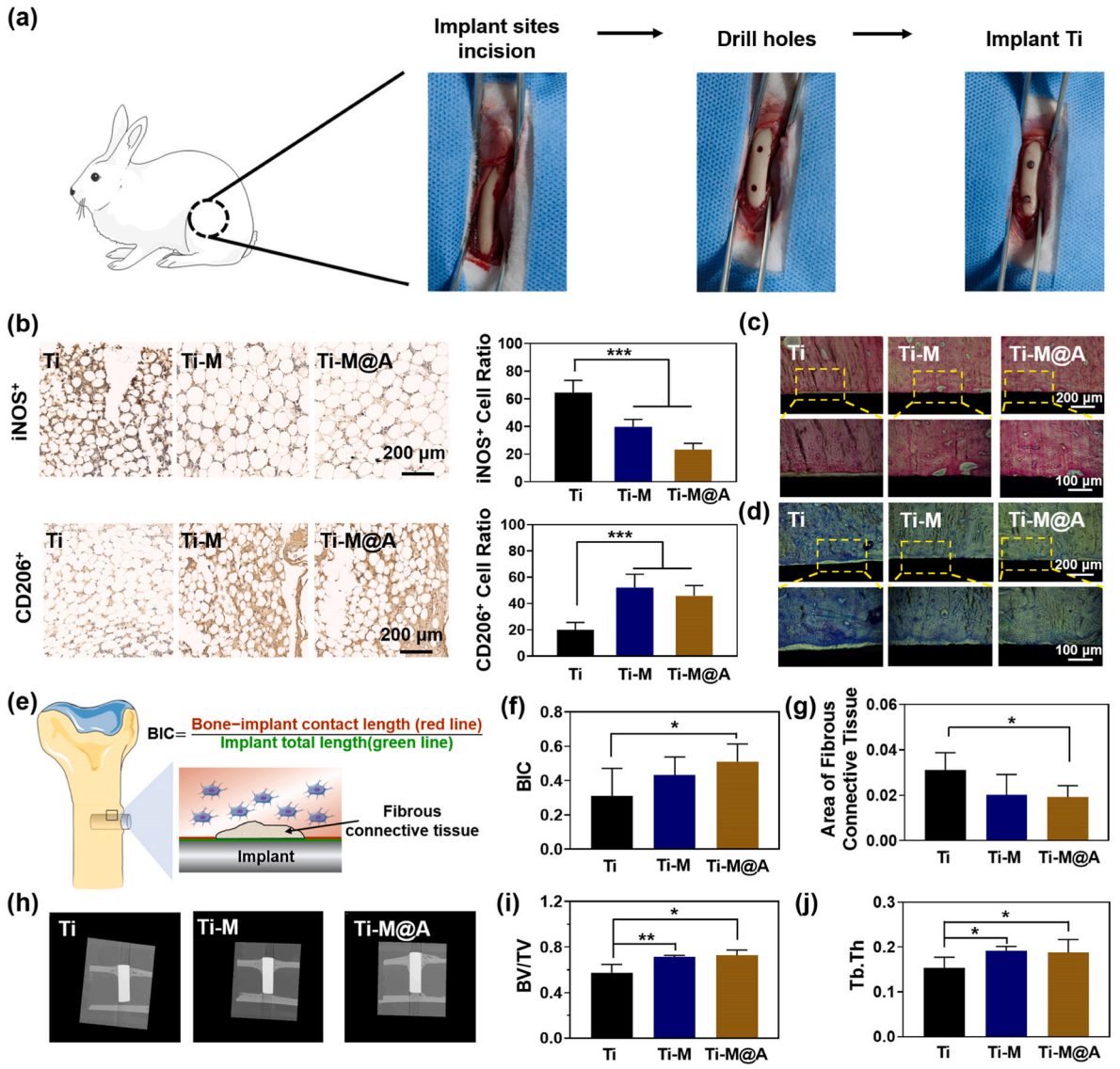

Fig. 6. *In vivo* osseointegration assay in a bone defect/non-infection model. (a) The surgical procedure of the *in vivo* rabbit animal model. (b) Immunohistochemical staining of anti-iNOS and CD206 antibodies and the quantitative analysis of the ratios of $iNOS^+$ and $CD206^+$ cells (n = 5). *** denotes $p < 0.001$. (c) to (d) Hard tissue section staining results: (c) methylene blue and basic fuchsin staining and (d) toluidine blue staining images. (e) Schematic for assessing the osseointegration of implants *in vivo* based on the results of methylene blue and basic fuchsin staining. Quantitative analysis of (f) BIC and (g) area of fibrous connective tissue at the interface between bone tissue and implant based on the results of methylene blue and basic fuchsin staining (n = 5). *denotes $p < 0.05$. (h) Micro-CT 2D reconstructed images of the lateral sections of the implant after 60 days of implantation. Quantitative analysis of (i) BV/TV and (j) Tb.Th through Micro-CT results (n = 3). *denotes $p < 0.05$, ** denotes $p < 0.005$. (For interpretation of the references to color in this figure legend, the reader is referred to the Web version of this article.)

pathogen biofilms on the surface of implants [46,47,59]. As reported, the antibiotic resistance of biofilms is 10–1000 times higher than that of planktonic bacteria [59,60]. Notably, the Ti-M@A we developed could strongly resist the formation of biofilms, therefore inhibit the infection efficiently.

A high density of antimicrobial agents, including AMPs, on the implant surface would produce cytotoxicity, limiting their application [28]. Herein, we demonstrated that the cytotoxicity of AMPs could be eliminated by hiding them in MSNs. Many studies have reported methods of hiding AMPs, such as covering them with polymers or mixing them into surface coatings directly [61,62]. Compared with these strategies, our functionalized surface realized the controlled release of the AMP, which helped to decrease toxicity while maintaining long-term surface activity.

In addition to shielding the toxicity of the AMP, the diselenide-bridged MSN on the surface further enhanced the osteogenic activity of the implants. This was because Se can protect stem cells from osteogenic differentiation inhibition and improve osteogenic activity by inhibiting oxidative stress [40]. Our results also demonstrated that when the microspheres did not contain Se, they did not possess osteogenic activity to *mBMSCs* on the surface of Ti-M(Se-), especially after 14 days of culture (Fig. S7). Additionally, we proved that Ti-M and Ti-M@A can regulate the polarization of macrophages to the M2 type and contribute to tissue healing because the Se in the MSNs can play an immunomodulatory role. For example, Zhu et al. prepared a Se-containing phycocyanin Se PC. Se PC can significantly reduce the extent of colitis in mice because Se inhibits NF-κB nuclear translocation to reduce the transcription of proinflammatory cytokines [63]. Therefore, Ti-M and Ti-M@A were expected to enhance tissue repair.

The *in vivo* assay showed that the Se-containing surfaces of Ti-M and Ti-M@A could promote osseointegration in a bone defect/non-infection model. There was no significant difference between the two surfaces, which indicated that the AMPs hidden in the MSNs did not have a negative effect on osteogenesis. However, Ti-M lost the effect of

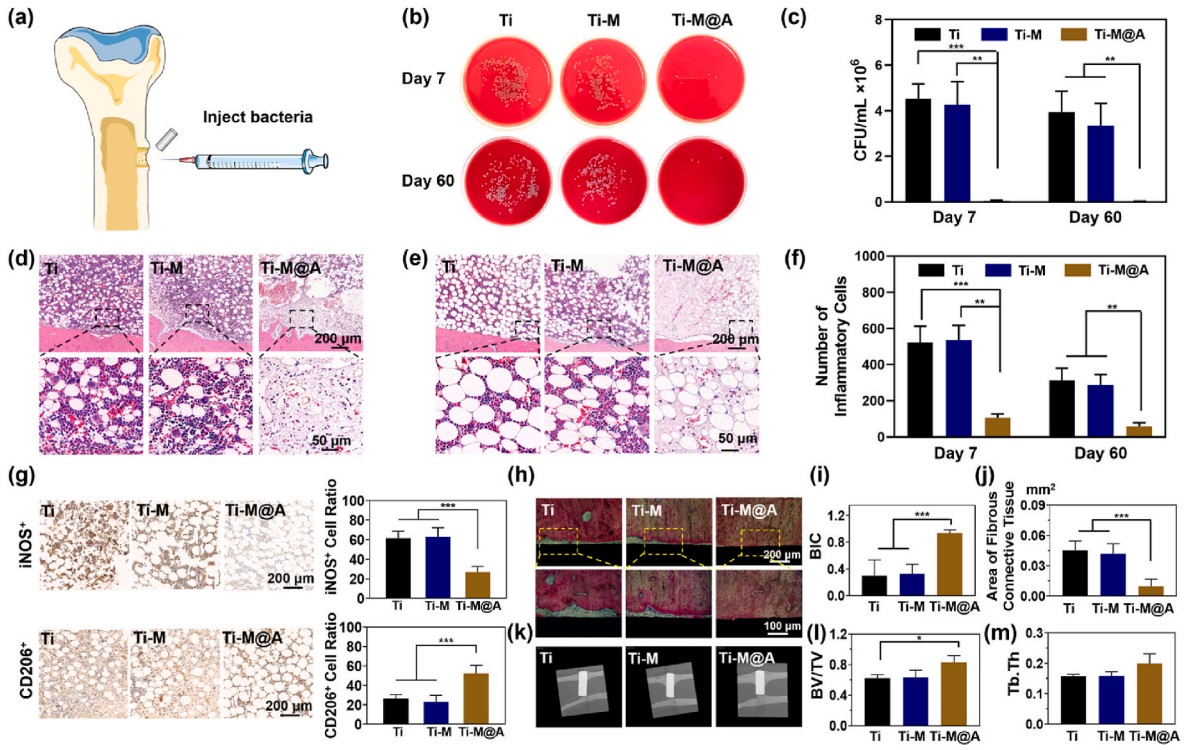

Fig. 7. *In vivo* assay in a bone defect/infection model. (a) The surgical procedure of the *in vivo* rabbit animal model. (b) The bacterial culture results of the indicated implants after 7 and 60 days of implantation. (c) Antimicrobial activity of the indicated implants after 7 and 60 days of implantation. The H&E staining images of the tissues around the implants after (d) 7 and (e) 60 days of implantation. The high-magnification images were taken from the black rectangles. (f) The quantification of inflammatory cells calculated from the H&E images after 7 and 60 days of implantation (n = 3). (g) Immunohistochemical staining of the hard tissue section of implantation with anti-iNOS and CD206 antibodies and the quantitative analysis of the ratios of $iNOS^+$ and $CD206^+$ cells (n = 5) *** denotes $p < 0.001$. (h) Images of methylene blue and basic fuchsin staining of the hard tissue section after 60 days of implantation. Quantitative analysis of (i) BIC and (j) area of fibrous connective tissue at the interface between bone tissue and implant from the methylene blue and basic fuchsin staining images (n = 5) ***denotes $p < 0.001$. (k) Micro-CT representative 2D reconstructed image of the lateral section after 60 days of implantation. Quantitative analysis of (l) BV/TV and (m) Tb.Th from the Micro-CT results (n = 3). *denotes $p < 0.05$. (For interpretation of the references to color in this figure legend, the reader is referred to the Web version of this article.)

promoting osseointegration in the bone defect/infection model, indicating the limitations of the functionalization with a single type of bioactivity. Moreover, Ti-M@A could exhibit excellent antibacterial activity and osseointegration simultaneously in the bone defect/infection model.

Finally, the sustained drug release system we built was universal and could be applied to control the release of other peptides, such as YGFGG. Clinical implants required various complex surface functionalities, and the universality of our system was expected to endow titanium-based implants with more functions.

5. Conclusions

In summary, we developed a bioactive orthopedic titanium implant based on diselenide-bridged MSNs that released the AMP in the sustained manner. After immobilization on the titanium implants, the MSN (M@A) exhibited long-term stability, mechanical stability, good sustained release performance and excellent bioactive properties. *In vitro* assays demonstrated that the functionalized Ti-M@A implant had excellent biocompatibility and antimicrobial, anti-inflammatory and osteogenic activities. *In vivo* experiments further showed that the Ti-M@A implant significantly inhibited bacterial infection and promoted osseointegration after 60 days of implantation in infection and non-infection models. These findings will provide an effective strategy for developing bioactive orthopedic titanium implants with efficient and safe antimicrobial activity and osseointegration.

CRediT authorship contribution statement

Jiyu Dong: Data curation, Writing - original draft, Formal analysis, Validation. **Fangman Chen:** Data curation, Formal analysis, Writing - original draft, Validation. **Yuying Yao:** Data curation, Formal analysis, Writing - review & editing, Validation. **Congcong Wu:** Data curation, Writing - review & editing. **Silin Ye:** Formal analysis, Validation, Writing - original draft. **Zunwei Ma:** Formal analysis, Validation. **Haipeng Yuan:** Formal analysis. **Dan Shao:** Conceptualization, Funding acquisition, Methodology, Project administration, Supervision, Writing - original draft. **Lin Wang:** Conceptualization, Funding acquisition, Investigation, Methodology, Project administration, Resources, Supervision, Writing - original draft, Writing - review & editing. **Yingjun Wang:** Conceptualization, Funding acquisition, Project administration, Supervision.

Declaration of competing interest

The authors declare the following financial interests/personal relationships which may be considered as potential competing interests: Yingjun Wang, Jiyu Dong, Lin Wang, Dan Shao has patent #202210242685.5 pending to South China University of Technology.

Data availability

Data will be made available on request.

Acknowledgments

This work was financially supported by National Key R&D Program of China (2023YFB3809901), Science and Technology Program of Guangzhou (202206040001), the Guangdong Natural Science Funds for Distinguished Young Scholars (2019B151502029) and the Fundamental Research Funds for the Central Universities.

Appendix A. Supplementary data

Supplementary data to this article can be found online at https://doi.org/10.1016/j.biomaterials.2023.122465.

References

[1] X. Liu, P.K. Chu, C. Ding, Surface modification of titanium, titanium alloys, and related materials for biomedical applications, Mater. Sci. Eng. R Rep. 47 (2004) 49–121.
[2] D. Suh, W.L. Jo, S.C. Kim, Y.S. Kim, S.Y. Kwon, Y.W. Lim, Comparative analysis of titanium coating on cobalt-chrome alloy in vitro and in vivo direct metal fabrication vs. plasma spraying, J. Orthop. Surg. Res. 15 (2020) 564.
[3] R. Tejero, E. Anitua, G. Orive, Toward the biomimetic implant surface: biopolymers on titanium-based implants for bone regeneration, Prog. Polym. Sci. 39 (2014) 1406–1447.
[4] X. Shen, Y. Hu, G. Xu, W. Chen, K. Xu, Q. Ran, et al., Regulation of the biological functions of osteoblasts and bone formation by Zn-incorporated coating on microrough titanium, ACS Appl. Mater. Interfaces 6 (2014) 16426–16440.
[5] Y. Zhao, H. Cao, H. Qin, T. Cheng, S. Qian, M. Cheng, et al., Balancing the osteogenic and antibacterial properties of titanium by codoping of Mg and Ag: an in vitro and in vivo study, ACS Appl. Mater. Interfaces 7 (2015) 17826–17836.
[6] David W. Grainger, Henny C. van der Mei, Paul C. Jutte, Jan J.A.M. van den Dungen, Marcus J. Schultz, Bernard F.A.M. van der Laan, Sebastian A.J. Zaat, J. Henk, Busscher Critical factors in the translation of improved antimicrobial strategies for medical implants and devices, Biomaterials 34 (37) (2013) 9237–9243.
[7] Ziyi Lu, Yueming Wu, Zihao Cong, Yuxin Qian, Xue Wu, Ning Shao, Zhongqian Qiao, Haodong Zhang, Yunrui She, Kang Chen, Hengxue Xiang, Bin Sun, Yu Qian, Yuan Yuan, Haodong Lin, Meifang Zhu, Runhui Liu, Effective and biocompatible antibacterial surfaces via facile synthesis and surface modification of peptide polymers, Bioact. Mater. 6 (12) (2021) 4531–4541.
[8] K. Rutledge-Taylor, A. Matlow, D. Gravel, J. Embree, N. Le Saux, L. Johnston, et al., A point prevalence survey of health care-associated infections in Canadian pediatric inpatients, Am. J. Infect. Control 40 (2012) 491–496.
[9] B. Allegranzi, S.B. Nejad, C. Combescure, W. Graafmans, H. Attar, L. Donaldson, et al., Burden of endemic health-care-associated infection in developing countries: systematic review and meta-analysis, Lancet 377 (2011) 228–241.
[10] R.O. Darouiche, Treatment of infections associated with surgical implants, N. Engl. J. Med. 350 (2004) 1422–1429.
[11] D. Campoccia, L. Montanaro, C.R. Arciola, A review of the biomaterials technologies for infection-resistant surfaces, Biomaterials 34 (2013) 8533–8554.
[12] Y. Apidianakis, M.N. Mindrinos, W. Xiao, G.W. Lau, R.L. Baldini, R.W. Davis, et al., Profiling early infection responses: Pseudomonas aeruginosa eludes host defenses by suppressing antimicrobial peptide gene expression, Proc Natl Acad Sci U S A 102 (2005) 2573–2578.
[13] J.M. Ghigo, Natural conjugative plasmids induce bacterial biofilm development, Nature 412 (2001) 442–445.
[14] J. Liao, W. Chen, M. Yang, J. Zhou, Z. Wang, Y. Zhou, et al., Conducting photopolymers on orthopeadic implants having a switch of priority between promoting osteogenic and antibacterial activity, Mater. Horiz. 5 (2018) 545–552.
[15] J. Raphel, M. Holodniy, S.B. Goodman, S.C. Heilshorn, Multifunctional coatings to simultaneously promote osseointegration and prevent infection of orthopaedic implants, Biomaterials 84 (2016) 301–314.
[16] Z. Yuan, P. Liu, Y. Hao, Y. Ding, K. Cai, Construction of Ag-incorporated coating on Ti substrates for inhibited bacterial growth and enhanced osteoblast response, Colloids Surf. B Biointerfaces 171 (2018) 597–605.
[17] Y. Li, L. Liu, P. Wan, Z. Zhai, Z. Mao, Z. Ouyang, et al., Biodegradable Mg-Cu alloy implants with antibacterial activity for the treatment of osteomyelitis: in vitro and in vivo evaluations, Biomaterials 106 (2016) 250–263.
[18] J.A. Lemire, J.J. Harrison, R.J. Turner, Antimicrobial activity of metals: mechanisms, molecular targets and applications, Nat. Rev. Microbiol. 11 (2013) 371–384.
[19] D. Hu, H. Li, B. Wang, Z. Ye, W. Lei, F. Jia, et al., Surface-adaptive gold nanoparticles with effective adherence and enhanced photothermal ablation of methicillin-resistant Staphylococcus aureus biofilm, ACS Nano 11 (2017) 9330–9339.
[20] S.M. Skovdal, N.P. Jorgensen, E. Petersen, S. Jensen-Fangel, R. Ogaki, G. Zeng, et al., Ultra-dense polymer brush coating reduces Staphylococcus epidermidis biofilms on medical implants and improves antibiotic treatment outcome, Acta Biomater. 76 (2018) 46–55.
[21] M. Kumar, S. Jaiswal, K.K. Sodhi, P. Shree, D.K. Singh, P.K. Agrawal, et al., Antibiotics bioremediation: perspectives on its ecotoxicity and resistance, Environ. Int. 124 (2019) 448–461.
[22] M.K. Kang, S.B. Lee, S.K. Moon, K.M. Kim, K.N. Kim, The biomimetic apatite-cefalotin coatings on modified titanium, Dent. Mater. J. 31 (2012) 98–105.
[23] R.F. Zhou, S.H. Shen, Y. Zhong, P. Liu, Y.Q. Zhang, L.J. Zhang, et al., Co-construction of advanced sulfur host by implanting titanium carbide into Aspergillus Niger spore carbon, Chinese Chem Lett 33 (2022) 3981–3986.
[24] Y. Lai, A.E. Villaruz, M. Li, D.J. Cha, D.E. Sturdevant, M. Otto, The human anionic antimicrobial peptide dermcidin induces proteolytic defence mechanisms in staphylococci, Mol. Microbiol. 63 (2007) 497–506.
[25] R.E.W. Hancock, Cationic peptides: effectors in innate immunity and novel antimicrobials, Lancet Infect. Dis. 1 (2001) 156–164.
[26] R.M. Epand, H.J. Vogel, Diversity of antimicrobial peptides and their mechanisms of action, Biochim. Biophys. Acta Biomembr. 1462 (1999) 11–28.
[27] J. Chen, X. Shi, Y. Zhu, Y. Chen, M. Gao, H. Gao, et al., On-demand storage and release of antimicrobial peptides using Pandora's box-like nanotubes gated with a bacterial infection-responsive polymer, Theranostics 10 (2020) 109–122.
[28] M. Kazemzadeh-Narbat, B.F. Lai, C. Ding, J.N. Kizhakkedathu, R.E. Hancock, R. Wang, Multilayered coating on titanium for controlled release of antimicrobial peptides for the prevention of implant-associated infections, Biomaterials 34 (2013) 5969–5977.
[29] Q. Yu, T. Deng, F.C. Lin, B. Zhang, J.I. Zink, Supramolecular assemblies of heterogeneous mesoporous silica nanoparticles to Co-deliver antimicrobial peptides and antibiotics for synergistic eradication of pathogenic biofilms, ACS Nano 14 (2020) 5926–5937.
[30] M. Godoy-Gallardo, C. Mas-Moruno, K. Yu, J.M. Manero, F.J. Gil, J. N. Kizhakkedathu, et al., Antibacterial properties of hLf1-11 peptide onto titanium surfaces: a comparison study between silanization and surface initiated polymerization, Biomacromolecules 16 (2015) 483–496.
[31] M. Li, D.J. Cha, Y. Lai, A.E. Villaruz, D.E. Sturdevant, M. Otto, The antimicrobial peptide-sensing system aps of Staphylococcus aureus, Mol. Microbiol. 66 (2007) 1136–1147.
[32] G.A. Hudalla, W.L. Murphy, Immobilization of peptides with distinct biological activities onto stem cell culture substrates using orthogonal chemistries, Langmuir 26 (2010) 6449–6456.
[33] M.K.S. Batista, M. Gallemí, A. Adeva, C.A.R. Gomes, P. Gomes, Facile regioselective synthesis of a novel chitosan–pexiganan conjugate with potential interest for the treatment of infected skin lesions, Synth. Commun. 39 (2009) 1228–1240.
[34] J. He, J. Chen, G. Hu, L. Wang, J. Zheng, J. Zhan, et al., Immobilization of an antimicrobial peptide on silicon surface with stable activity by click chemistry, J. Mater. Chem. B 6 (2018) 68–74.
[35] Z.X. Tu, Y.L. Zhong, H.Z. Hu, D. Shao, R.N. Haag, M. Schirner, et al., Design of therapeutic biomaterials to control inflammation, Nat. Rev. Mater. 7 (2022) 557–574.
[36] D.Z. Ma, H. Shen, F.M. Chen, W.Y. Liu, Y.N. Zhao, Z.F. Xiao, et al., Inflammatory microenvironment-responsive nanomaterials promote spinal cord injury repair by targeting IRF5, Adv Healthc Mater 11 (2022) DOI10.1002/adhm.202201319.
[37] J. Xu, J. Xu, T. Shi, Y. Zhang, F. Chen, C. Yang, et al., Probiotic-inspired nanomedicine restores intestinal homeostasis in colitis by regulating redox balance, immune responses, and the gut microbiome, Advanced materials (2022) e2207890.
[38] C.X. Shi, J. Dawulieti, F.Y. Shi, C. Yang, Q. Qin, T.F. Shi, et al., A nanoparticulate dual scavenger for targeted therapy of inflammatory bowel disease, Sci. Adv. 8 (2022).
[39] D. Shao, F. Zhang, F. Chen, X. Zheng, H. Hu, C. Yang, et al., Biomimetic diselenide-bridged mesoporous organosilica nanoparticles as an X-ray-responsive biodegradable carrier for chemo-immunotherapy, Advanced materials 32 (2020) e2004385.
[40] L. Hongmei, B. Weixia, L. Songxiu, H. Kaixun, Selenium protects bone marrow stromal cells against hydrogen peroxide-induced inhibition of osteoblastic differentiation by suppressing oxidative stress and ERK signaling pathway, Biol. Trace Elem. Res. 150 (2012) 441–450.
[41] D. Shao, M. Li, Z. Wang, X. Zheng, Y.H. Lao, Z. Chang, et al., Bioinspired diselenide-bridged mesoporous silica nanoparticles for dual-responsive protein delivery, Adv Mater (2018) e1801198.
[42] J. Peng, F. Chen, Y. Liu, F. Zhang, L. Cao, Q. You, et al., A light-driven dual-nanotransformer with deep tumor penetration for efficient chemo-immunotherapy, Theranostics 12 (2022) 1756–1768.
[43] Y. Yang, F. Chen, N. Xu, Q. Yao, R. Wang, X. Xie, et al., Red-light-triggered self-destructive mesoporous silica nanoparticles for cascade-amplifying chemo-photodynamic therapy favoring antitumor immune responses, Biomaterials 281 (2022) 121368.
[44] X. Ding, W. Chin, C.N. Lee, J.L. Hedrick, Y.Y. Yang, Peptide-functionalized polyurethane coatings prepared via grafting-to strategy to selectively promote endothelialization, Adv Healthc Mater 7 (2018).
[45] Z. Shutao, Y. Hongtao, W. Minqi, Diego Mantovani, Y. Ke, Witte Frank, T. Lili, Y. Bing, Q. Xinhua, Immunomodulatory biomaterials against bacterial infections: progress, challenges, and future perspectives, Innovation 4 (6) (2023) 100503.
[46] J.G. Silva Souza, M.M. Bertolini, R.C. Costa, B.E. Nagay, A. Dongari-Bagtzoglou, V. A. Ricardo Barao, Targeting implant-associated infections: titanium surface loaded with antimicrobial, iScience 24 (2021).
[47] C. von Eiff, B. Jansen, W. Kohnen, K. Becker, Infections associated with medical devices - pathogenesis, management and prophylaxis, Drugs 65 (2005) 179–214.
[48] Z. Tu, Y. Zhong, H. Hu, D. Shao, R. Haag, M. Schirner, et al., Design of therapeutic biomaterials to control inflammation, Nat. Rev. Mater. 7 (2022) 557–574.
[49] Q. He, S. Yuan, H. Tang, S. Wang, Z. Mu, D. Li, et al., Safeguarding osteointegration in diabetic patients: a potent "chain armor" coating for scavenging ROS and

macrophage reprogramming in a microenvironment-responsive manner, Adv. Funct. Mater. (2021) 31.
[50] Y. Weiling, C. Miao, B. Jiaxiang, X. Yaozeng, W. Miao, G. Dechun, P. Guoqing, Recent advances in orthopedic polyetheretherketone biomaterials: material fabrication and biofunction establishment, Smart Materials in Medicine 3 (2022) 20–36.
[51] S.R. Meyers, M.W. Grinstaff, Biocompatible and bioactive surface modifications for prolonged in vivo efficacy, Chem. Rev. 112 (2012) 1615–1632.
[52] R. Chen, M.D. Willcox, K.K. Ho, D. Smyth, N. Kumar, Antimicrobial peptide melimine coating for titanium and its in vivo antibacterial activity in rodent subcutaneous infection models, Biomaterials 85 (2016) 142–151.
[53] D. Liu, Y. Xi, S. Yu, K. Yang, F. Zhang, Y. Yang, T. Wang, S. He, Y. Zhu, Z. Fan, J. Du, A polypeptide coating for preventing biofilm on implants by inhibiting antibiotic resistance genes, Biomaterials 293 (2023) 121957.
[54] Y. Zhao, B.G. Trewyn, I.I. Slowing, V.S. Lin, Mesoporous silica nanoparticle-based double drug delivery system for glucose-responsive controlled release of insulin and cyclic AMP, J. Am. Chem. Soc. 131 (2009) 8398–8400.
[55] X. Chen, Y. Liu, A. Lin, N. Huang, L. Long, Y. Gang, J. Liu, Folic acid-modified mesoporous silica nanoparticles with pH-responsiveness loaded with Amp for an enhanced effect against anti-drug-resistant bacteria by overcoming efflux pump systems, Biomater. Sci. 6 (2018) 1923–1935.
[56] Z. Ma, H. Wang, Z. Shi, F. Yan, Q. Li, J. Chen, Z.K. Cui, Y. Zhang, X. Jin, Y.G. Jia, L. Wang, Inhalable GSH-triggered nanoparticles to treat commensal bacterial infection in in situ lung tumors, ACS Nano 17 (2023) 5740–5756.
[57] Zhuqing Wan, Qinyuan Dong, Yunsong Liu, Xiao Zhang, Ping Zhang, Longwei Lv, Yongsheng Zhou, Programmed biomolecule delivery orchestrate bone tissue regeneration via MSC recruitment and epigenetic modulation, Chem. Eng. J. 438 (2022) 135518.
[58] B. Li, T.J. Webster, Bacteria antibiotic resistance: new challenges and opportunities for implant-associated orthopedic infections, J. Orthop. Res. 36 (2018) 22–32.
[59] C. von Eiff, B. Jansen, W. Kohnen, K. Becker, Infections associated with medical devices, Drugs 65 (2005) 179–214.
[60] A.W. Smith, Biofilms and antibiotic therapy: is there a role for combating bacterial resistance by the use of novel drug delivery systems? Adv. Drug Deliv. Rev. 57 (2005) 1539–1550.
[61] H. Yazici, M.B. O'Neill, T. Kacar, B.R. Wilson, E.E. Oren, M. Sarikaya, et al., Engineered chimeric peptides as antimicrobial surface coating agents toward infection-free implants, ACS Appl. Mater. Interfaces 8 (2016) 5070–5081.
[62] H. Chouirfa, H. Bouloussa, V. Migonney, C. Falentin-Daudre, Review of titanium surface modification techniques and coatings for antibacterial applications, Acta Biomater. 83 (2019) 37–54.
[63] C. Zhu, Q. Ling, Z. Cai, Y. Wang, Y. Zhang, P.R. Hoffmann, et al., Selenium-containing phycocyanin from Se-enriched spirulina platensis reduces inflammation in dextran sulfate sodium-induced colitis by inhibiting NF-kappaB activation, J. Agric. Food Chem. 64 (2016) 5060–5070.